Nanoscale

PAPER

View Article Online
View Journal | View Issue

Cite this: *Nanoscale*, 2015, **7**, 190

808 nm driven Nd^{3+}-sensitized upconversion nanostructures for photodynamic therapy and simultaneous fluorescence imaging†

Dan Wang,‡[a,b] Bin Xue,‡[a,b] Xianggui Kong,*[a] Langping Tu,[a,b] Xiaomin Liu,[a] Youlin Zhang,[a] Yulei Chang,[a] Yongshi Luo,[a] Huiying Zhao[c] and Hong Zhang*[d]

Received 26th August 2014,
Accepted 27th October 2014

DOI: 10.1039/c4nr04953e

www.rsc.org/nanoscale

The *in vivo* biological applications of upconversion nanoparticles (UCNPs) prefer excitation at 700–850 nm, instead of 980 nm, due to the absorption of water. Recent approaches in constructing robust Nd^{3+} doped UCNPs with 808 nm excitation properties rely on a thick Nd^{3+} sensitized shell. However, for the very important and popular Förster resonance energy transfer (FRET)-based applications, such as photodynamic therapy (PDT) or switchable biosensors, this type of structure has restrictions resulting in a poor energy transfer. In this work, we have designed a $NaYF_4$:Yb/Ho@$NaYF_4$:Nd@$NaYF_4$ core–shell–shell nanostructure. We have proven that this optimal structure balances the robustness of the upconversion emission and the FRET efficiency for FRET-based bioapplications. A proof of the concept was demonstrated for photodynamic therapy and simultaneous fluorescence imaging of HeLa cells triggered by 808 nm light, where low heating and a high PDT efficacy were achieved.

1. Introduction

Lanthanide-doped upconversion nanoparticles (UCNPs) have been variously and elaborately designed[1–6] because they provide many potential applications in bioimaging, drug delivery, sensors, data storage,[7–10] and, in particular, distance-dependent Förster resonance energy transfer (FRET, also referred to as luminescence resonance energy transfer (LRET))-based applications such as molecular photo-switches, biosensing and photodynamic therapy (PDT).[11–13] For *in vivo* bioapplications, upconversion nanoparticles that are excitable at 980 nm have previously been the focus. This is because this excitation wavelength falls in the so-called "optical window" of tissue and the biological environment is hardly excited, leading to high quality as well as relatively deep depth imaging. However, 980 nm is at the rising edge of the absorption of tissue (although much lower than visible light) and can be absorbed by water. As a consequence, overheating effects limit the power of the excitation light.[14]

Various efforts have been made to improve the performance of upconversion nanomaterials in this regard. Recently, Nd^{3+}-sensitized UCNPs with 800 nm laser excitation properties were reported. Han *et al.* found that triply doping Nd^{3+}, Yb^{3+} and an activator in $NaYF_4$ could result in an upconversion emission under excitation at 800 nm.[15] Yb^{3+} ions act as a bridge to transfer the energy from the Nd^{3+} ions to the activators. For the triple doping in $NaYF_4$, due to quenching effects between the activators and Nd^{3+} ions, the upconversion emission was very weak. Several groups spatially separated activators from Nd^{3+} ions *via* core–shell structures to acquire high efficient luminescence under excitation at 800 nm.[16–19] Although the upconversion luminescence (UCL) caused by a thick Nd^{3+} sensitizing shell could be used for bioimaging, this structure is not appropriate for FRET-based applications, such as homogeneous bioassays, biosensing and PDT, which are in general based on an energy transfer mechanism. For example, for UCNP-based PDT, the luminescence activators inside the nanoparticles (as the energy donors) transfer the excitation energy to the acceptors, *i.e.* the photosensitizing molecules (photosensitizers), to generate cytotoxic singlet oxygen ($^1O_2$, type II) to kill cancer cells. The energy transfer rate depends strongly on the distance between the donors (activators) and the acceptors (photosensitizers).[20] Although spatially separating the activators and Nd^{3+} ions could result in a higher UCL efficiency, this Nd^{3+} sensitizer layer may lead to a large distance between the activators

[a]*State Key Laboratory of Luminescence and Applications, Changchun Institute of Optics, Fine Mechanics and Physics, Chinese Academy of Sciences, Changchun 130033, China. E-mail: xgkong14@ciomp.ac.cn*
[b]*Graduate University of the Chinese Academy of Sciences, Beijing 100049, China*
[c]*Department of Basic Medicine, Gerontology Department of First Bethune Hospital, University of Jilin, Changchun 130021, China*
[d]*Van't Hoff Institute for Molecular Sciences, University of Amsterdam, Science Park 904, 1098 XH Amsterdam, The Netherlands. E-mail: h.zhang@uva.nl*
†Electronic supplementary information (ESI) available: TEM images, XRD patterns and NIR emission spectra of UCNPs. See DOI: 10.1039/c4nr04953e
‡These authors contributed equally to this work.

and photosensitizers, which is not favorable for the FRET process in PDT. Moreover, in contrast to bioimaging, PDT requires a higher upconversion efficiency because it performs under irradiation of a lower power density. Since spatial separation of the activators from the Nd^{3+} ions is essential for high upconversion luminescence efficiency, the challenge for FRET-based biological applications is how to achieve a high UCL efficiency and an effective FRET under excitation at ~800 nm.

In this work we have overcome the difficulty by balancing a high UCL efficiency and a high FRET efficiency *via* the construction of a novel $NaYF_4$:Yb/Ho@$NaYF_4$:Nd@$NaYF_4$ core–shell–shell structure. A proof of concept is demonstrated for its use in FRET-based PDT applications. The outermost inert layer was to improve the UCL to compensate for the UCL deleterious effect due to the decreased Nd^{3+}-sensitized layer. By using this novel nanostructure, PDT without overheating effects and simultaneous UCL imaging under excitation at 808 nm was realized.

2. Experimental section

2.1 Materials

$NdCl_3{\cdot}6H_2O$ (99.9%), $HoCl_3{\cdot}6H_2O$ (99.9%), $YbCl_3{\cdot}6H_2O$ (99.9%), $YCl_3{\cdot}6H_2O$ (99.9%), oleic acid (90%) (OA), 1-octadecene (90%) (ODE), $Y(CF_3COO)_3$, $Yb(CF_3COO)_3$, CF_3COONa, Rose Bengal, hexanoic acid, poly(allylamine) (PAAm), dimethyl formamide (DMF), mPEG-succinimidyl carbonate(MPEG-SC), 1-ethyl-3-(3-dimethylaminopropy) carbodiimide (EDC), *N*-hydroxy-succinimide (NHS) and 1,3-diphenylisobenzofuran (DPBF) were all purchased from Sigma-Aldrich. $Nd(CF_3COO)_3$ and $Ho(CF_3COO)_3$ were made from Nd_2O_3 and Ho_2O_3 in excess CF_3COOH and then CF_3COOH was evaporated. Paraformaldehyde (4%) and 4′,6-diamidino-2-phenylindole (DAPI) were purchased from Beyotime Institute of Biotechnology. NaOH, NH_4F and dimethyl formamide were purchased from Beijing Chemical Works. All other chemical reagents were of analytical grade and were used directly without further purification.

2.2 Synthesis of β-$NaYF_4$:Yb/Ho(8/1%)@$NaYF_4$:Nd(20%)@$NaYF_4$ core–shell–shell nanoparticles

β-$NaYF_4$:Yb/Ho(8/1%)@$NaYF_4$:Nd(20%)@$NaYF_4$ core–shell–shell nanoparticles were synthesized based on a previously reported procedure.[21] $YbCl_3{\cdot}6H_2O$ (99.9%, 0.04 mmol), $YCl_3{\cdot}6H_2O$ (99.9%, 0.445 mmol) and $HoCl_3{\cdot}6H_2O$ (99.9%, 0.005 mmol) were dissolved in 3 mL of OA and 7.5 mL of ODE. The mixture was heated at 150 °C under argon protection. NH_4F (2 mmol) and NaOH (1.25 mmol) were dissolved in 5 mL of methanol and added to the three necked flask. Afterwards, the solution was heated to 70 °C to remove the methanol and subsequently heated to 300 °C for 1 hour. After that, 1 mmol of $NaYF_4$:Nd (20%) active shell in octadecene was injected into the reaction mixture and ripened for 10 min, and then the materials for another $NaYF_4$ inert shell (1 mmol) were added and ripened for 10 min. Finally, the solution was cooled down to room temperature and precipitated using ethanol. The solid was collected by centrifugation and dispersed in 6 mL of hexane.

The synthesis of different thicknesses of the active shell in β-$NaYF_4$:Yb/Ho(8/1%)@$NaYF_4$:Nd(20%)@$NaYF_4$ core–shell–shell nanoparticles was carried out exactly as outlined for the β-$NaYF_4$:Yb/Ho(8/1%)@$NaYF_4$:Nd (20%)@$NaYF_4$ nanoparticles above, except that the amount of injected small sacrifice nanoparticles (SNPs), α-NaYF4:Nd(20%), was 0.05 mmol, 0.1 mmol, 0.3 mmol or 0.5 mmol. After that, 0.1 mmol, 0.15 mmol, 0.17 mmol or 0.2 mmol of inert $NaYF_4$ shell was injected and ripened for 5 minutes.

2.3 Synthesis of amino-functionalized UCNPs

To obtain amino-functionalized UCNPs, a ligand exchange approach was adopted using PAAm to transform the hydrophobic UCNPs into hydrophilic ones. 50 μL (20 wt%) of PAAm was diluted with 4 mL of CH_3CH_2OH, then the UCNPs (200 μL, 2 mg mL^{-1}) were added to the PAAm solution, subjected to ultrasound for 2 minutes, and stirred for 24 hours at room temperature. After centrifugation twice, the products were dispersed in water for further functionalization.

2.4 Covalent conjugation of UCNPs with Rose Bengal

To compare the $^1O_2$ generation from four different thicknesses of active-shell UCNPs, covalent conjugation of the UCNPs with Rose Bengal was carried out in a similar way to Liu *et al.*[23] with a little modification. Rose Bengal hexanoic acid (RB) was obtained according to ref. 24. In order to covalently conjugate RB to amino-functionalized UCNPs, 4 mL of dimethyl formamide solution containing 0.2 mg of RB, 2 mg of EDC and 0.5 mg of NHS were incubated for 30 min, and then 20 mg of amino-functionalized UCNPs were added into the solution and left to react for 16 h. Then the UCNPs–RB were centrifuged with deionized water three times and redispersed in PBS solution. From the RB absorption spectrum, about 38 RB molecules were covalently conjugated on one nanoparticle.

2.5 Singlet oxygen determination

DPBF was used to determine the singlet oxygen generation.[25] In a typical DPBF experiment, 10 μL of a DPBF–ethanol solution (8 mM) was added to 2 mL of UCNPs–RB solution. Then the whole solution was irradiated using 808 nm laser light at the same power density (0.67 W cm^{-2}), and the absorption of DPBF at 417 nm was measured every 2 minutes. The procedure was the same for the $^1O_2$ detection experiments with the different active shell thicknesses.

2.6 Number of coupling RB molecules

The number of coupling RB molecules was calculated from the RB absorption spectrum. In a typical experiment, 10 μL, 20 μL, 30 μL, 40 μL, 50 μL or 60 μL of RB solution (10 mg mL^{-1}), 2 mg of EDC and 0.4 mg of NHS were added to 0.5 mL of UCNPs (10 mg mL^{-1}) solution and stirred for 16 h at room temperature. Then they were washed with DMF three times before measuring the UV-Vis absorption.

2.7 UCNPs were covalently functionalized with FA and PEG-SC

In order to specifically target cancer cells, FA was introduced covalently to UCNPs–RB. In a typical experiment, 2 mg of FA, 1 mg of PEG-SC, 2 mg of EDC, 0.5 mg of NHS and 10 mg of UCNPs–RB were added to 5 mL of DMF. The mixture was stirred for 12 h, centrifuged and then dispersed in PBS solution.

2.8 Comparing the overheating effects of an 808 nm laser and a 980 nm laser

In order to further verify the overheating effects induced by 808 nm and 980 nm lasers, HeLa cells were seeded into two 96-well plates at a concentration of 10^4 cells per well (100 μL) and then incubated for 24 hours at 37 °C under 5% CO_2. The cells were then exposed to an 808 nm laser and a 980 nm laser at different power densities of 0.67 W cm^{-2}, 1.15 W cm^{-2} and 1.62 W cm^{-2}. The cells were then incubated for 24 h. The MTT solution (5 mg mL^{-1}, 20 μL) was then added and incubated for 4 h, and then replaced with 150 μL of DMSO in each well. The absorbance in each well was measured at 492 nm. The cell viability was calculated using the following formula: cell viability = (mean absorbance of test wells − mean absorbance of medium control wells)/(mean absorbance of untreated wells − mean absorbance of medium control wells) × 100%.

2.9 MTT assays for cytotoxicity

The cytotoxity of UCNPs–RB was evaluated using HeLa cancer cells. The cells were seeded in 96-well plates (1×10^4 cells per well). After cultivation for 24 h, 100 μL of UCNPs–RB of different concentrations (0, 50, 100, 150, 200, 400 or 600 μg mL^{-1}) were added into the wells and incubated for 48 h. Then, MTT solution (20 μL, 5 mg mL^{-1}) was added into each well. After incubation for 4 h at 37 °C, the MTT solution was replaced with 150 μL of DMSO in each well. The absorbance in each well was measured at 492 nm.

2.10 *In vitro* cancer cell imaging

In our experiment, HeLa cells and A549 cells were seeded into three culture dishes at a concentration of 10^4 cells per culture dish (100 μL) and incubated for 24 hours at 37 °C under 5% CO_2. Then, the HeLa cells were cultured in RPMI-1640 medium incubated with FA and PEG-SC functionalized UCNPs–RB (200 μg mL^{-1}, 100 μL), and these were used as the positive group. HeLa cancer cells cultured in folate-free RPMI medium incubated with UCNPs–RB (200 μg mL^{-1}, 100 μL) was used as the control group.

In another control group, we used A549 cells incubated with FA and PEG-SC functionalized UCNPs–RB at the same concentration. All the cells were incubated for 4 h, and then washed with phosphate buffered saline (PBS) solution to fully remove any excess UCNPs–RB nanoconstructs. The cells were fixed by added paraformaldehyde (4 wt%, 1 mL) in each culture dish for 10 minutes. The cell nuclei were stained with DAPI (1 mL per culture dish) for 10 minutes. After washing five times with PBS solution, the cells were imaged using a laser confocal microscope (Nikon Confocal Microscope C2/C2si). UCL imaging of UCNPs–RB was performed using a confocal microscope equipped with an external 808 nm laser.

2.11 *In vitro* PDT

100 μL of HeLa cells were seeded into a 96-well plate at a concentration of 10^4 cells per well, and then incubated for 24 hours at 37 °C under 5% CO_2. After that, the cells were incubated with FA and PEG-SC functionalized UCNPs–RB of different concentrations (0, 50, 100, 150, 200, 400 or 600 μg mL^{-1}) for another 24 h, and then the cells were washed with PBS solution to remove unbound UCNPs–RB nanoconstructs. After irradiated for 10 min by an 808 nm laser at a power density of 0.67 W cm^{-2}, the cells were incubated for 4 h at 37 °C, incubated for 2 h, then the medium was removed and they were washed with PBS solution. The MTT solution (5 mg mL^{-1}, 20 μL) was added and the cells were incubated for 4 h. The MTT solution was then replaced with 150 μL of DMSO in each well. The absorbance in each well was measured at 492 nm.

2.12 General sample characterizations

The transmission electron microscopy (TEM) measurements were carried out using a JEM-2100F electron microscope operating at 200 KV. X-ray diffraction (XRD) measurements were performed with a Rigaku D/max-2000 diffractometer using Cu Kα radiation (λ = 1.5406 Å). Ultraviolet-visible (UV) absorption measurements were recorded using an UV-3101 spectrophotometer. The upconversion spectra were recorded at room temperature with a Maya 2000 visible spectrometer (Ocean optics) with the excitation source adapted to 808 nm fiber coupled diode lasers. NIR emission spectra were obtained with a TRIAX 550 spectrometer under excitation using 808 nm diode lasers. Luminescence digital photographs were taken with a SONY digital camera. The cells were imaged in bright field and fluorescence field using a NIKON confocal microscope C2-SI equipped with an 808 nm NIR laser.

3. Results and discussion

The designed core–shell–shell nanostructure that can be excited by an 808 nm laser is illustrated in Fig. 1a. These hexagonal-phase $NaYF_4$:Yb/Ho@$NaYF_4$:Nd@$NaYF_4$ core–shell–shell nanoparticles were synthesized according to a previous report with certain modifications (ESI, Experimental section and Fig. S1 and S2†).[21] To enhance the upconversion emission, a $NaYF_4$ inert layer was coated on the outermost layer to avoid the excitation energy loss in the nanosystem. Ho^{3+} ions (activators) were embedded in the core and Nd^{3+} ions were present in the shell layer to harvest the 808 nm light. Under excitation using 808 nm light, the UCL was achieved by an initial energy transfer from Nd^{3+} to Yb^{3+}. Due to the highly efficient energy transfer from Nd^{3+} to Yb^{3+}, the emission of Yb^{3+} ions at 975 nm ($^2F_{5/2} \rightarrow {}^2F_{7/2}$) was enhanced 47.4 times by the shell

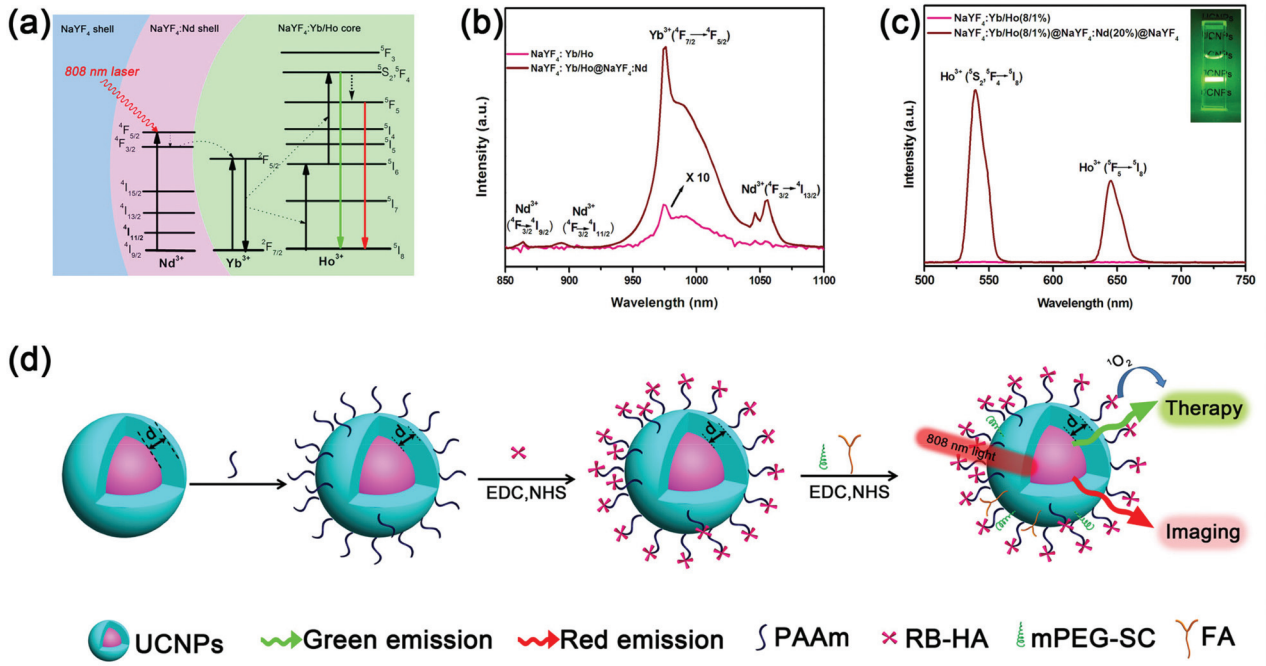

Fig. 1 (a) Upconversion mechanism of the nanostructure excited using an 808 nm laser. (b) NIR emission spectra of $NaYF_4$:Yb/Ho(8/1%) nanoparticles and $NaYF_4$:Yb/Ho(8/1%)@$NaYF_4$:Nd(20%) nanoparticles. (c) Room-temperature upconversion emission spectra of $NaYF_4$:Yb/Ho(8/1%) nanoparticles and $NaYF_4$:Yb/Ho(8/1%)@$NaYF_4$:Nd(20%)@$NaYF_4$ nanoparticles. (d) The construction and operating principle of the nanoplatform for photodynamic therapy and imaging.

under excitation at 808 nm (Fig. 1b). Consequently, the Yb^{3+} ions transferred the energy to the Ho^{3+} ions under the classical energy transfer upconversion (ETU) framework. Here, the bright green UC emission (Fig. 1c) at 540 nm ($^5S_2/^5F_4 \rightarrow {}^5I_8$) and the red UC emission at 650 nm ($^5F_5 \rightarrow {}^5I_8$) of Ho^{3+} can be observed and these emissions can used for PDT and bio-imaging, respectively (Fig. 1d). It was observed that a weak emission of Yb^{3+} was present when the bare core of the $NaYF_4$: Yb/Ho nanoparticles was excited with an 808 nm laser (Fig. 1b). Ho^{3+} ions ($^5I_8 \rightarrow {}^5I_4$) have a weak absorption near 808 nm,[22] which results in the population of $^5I_4$ when excited at 808 nm. After following the multiphonon relaxation from $^5I_4 \rightarrow {}^5I_5$, Ho^{3+} ions may transfer the excitation energy to Yb^{3+} ions, which gives rise to the weak emission of Yb^{3+}.

When a nanostructure is used for PDT and other FRET-based applications, the UCL should be as high as possible. The $NaYF_4$ inert layer effectively enhances the UCL by suppressing the surface quenching effects.[26] As is well known, the UCL intensity, I, for a two photon process is nearly proportional to the square of the absorbed excitation power density, I_{ex}. Therefore, increasing the excitation power density by a small amount will result in a big enhancement in the UCL (Fig. S3†). Coating the inert shell helps to transfer more energy from the Nd^{3+} ions (especially at the surface) to the Yb^{3+} ions. This results in a further increase in the excitation of Yb^{3+}, which is equivalent to the increase in the excitation power, enhancing the UCL effectively. It was observed that coating a 1.5 nm thick $NaYF_4$ inert layer efficiently enhanced the UCL (Fig. S4†). The UCL intensity increase was close to saturation for a thicker inert layer.

More importantly, we found that the inert shell could enhance the UCL more effectively when the thickness of the active Nd^{3+} layer was thin. Fig. 2d shows that the UCL was enhanced 15.1, 6.08 and 2.9 times when the thickness of the active layer was 0.5 nm, 1.5 nm and 4.2 nm, respectively. These results indicate that the enhance factor of the UCL was larger when the active layer was thinner. This can be explained by the fact that Nd^{3+} ions in a thicker active layer need more transfer steps from the Nd^{3+} ions on the outermost surface to the Yb^{3+} ions in the core (Fig. 2a and b), which will lower the enhance ability of the inert layer. This can be further confirmed by the fact that the enhance ability of the inert layer decreased with the concentration of Nd^{3+} ions. Fig. 2e–f show the enhance factor decreased from 4.01 to 2.53 when the concentration of Nd^{3+} ions increased from 10% to 50% (the active layer was ~5 nm). This is because when the concentration of Nd^{3+} ions increased, the separation between Nd^{3+} ions was shortened. So when we kept the shell thickness constant, the increased excitation energy by the inert layer also needed more transfer steps to the inner core (Fig. 2b and c). This could be further confirmed by the larger enhance factor of the NIR stokes emission of Yb^{3+} (Fig. S5 and S6†), where the number of transfer steps was less. So when the number of transfer steps is lower, the inert layer can more effectively enhance the UCL intensity.

This effect is very useful because when UCNPs are used as donors for PDT or other FRET-based applications, the active

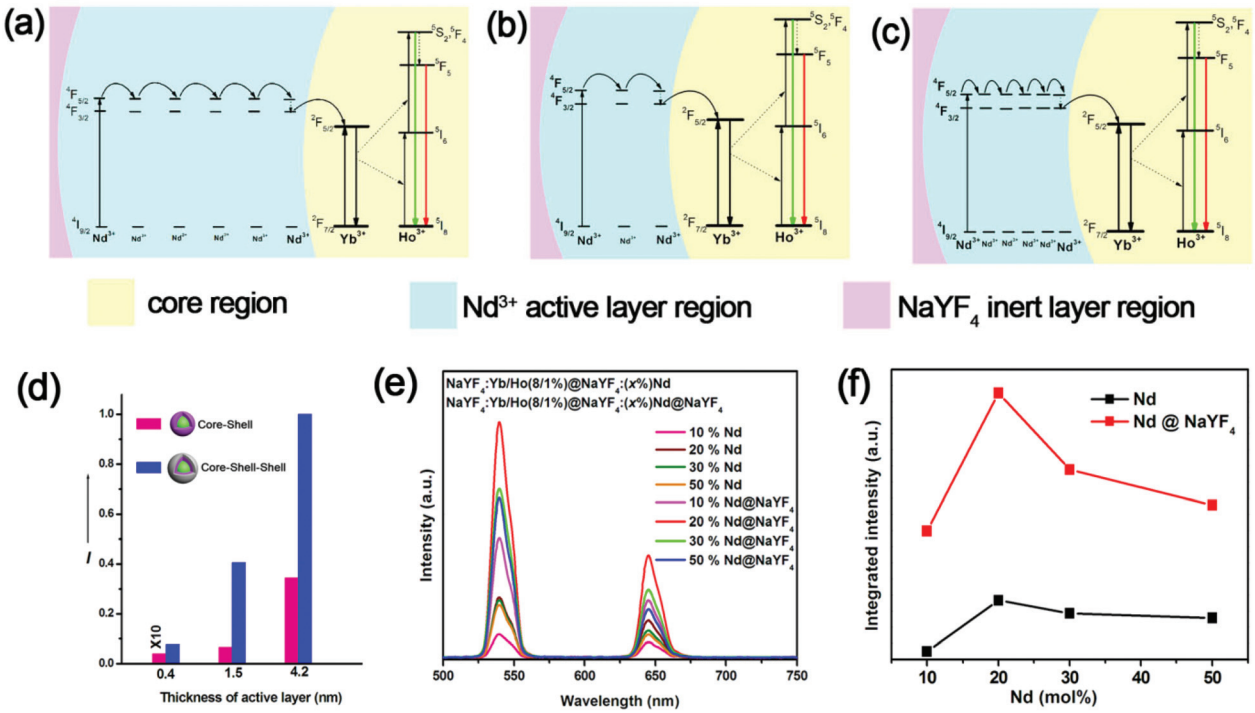

Fig. 2 Proposed energy transfer mechanisms of nanoparticles with (a) a thick active layer, (b) a thin active layer, (c) a high concentration of Nd^{3+} ions in the thin active layer. (d) UC emission intensity comparison of $NaYF_4$:Yb/Ho(8/1%)@$NaYF_4$:Nd(20%) nanoparticles with different active layer thicknesses (0.4 nm, 1.5 nm and 4.2 nm), with and without a thin inert protection layer ($NaYF_4$) in cyclohexane solution (20 mg ml^{-1}). (e) Room-temperature upconversion emission spectra of $NaYF_4$:Yb/Ho(8/1%)@$NaYF_4$:Nd(*x*%) (*x* = 10, 20, 30, 50) and $NaYF_4$:Yb/Ho(8/1%)@$NaYF_4$:xNd@$NaYF_4$ (*x* = 10, 20, 30, 50) under excitation at 808 nm (20 mg ml^{-1}). (f) Integrated intensity of the upconversion emission as a function of Nd^{3+}. The spectra were recorded under excitation by an 808 nm continuous-wave laser.

layer should be as thin as possible to increase the energy transfer efficiency between the activators and outermost acceptors. For the thinner active shell, the UCL will be weaker owing to the relatively lower light absorption from smaller amounts of Nd^{3+} ions in the thin sensitizer layer. Fortunately, the thin inert shell (1.5 nm) can significantly strengthen the UCL in this case. The UCL of nanostructures with an overall thickness of 3 nm (1.5 nm active layer + 1.5 nm inert layer) was even higher than for nanostructures with only an active layer of 4.2 nm (Fig. 2d). This indicates that our designed nanostructure (active layer + inert layer) will have a higher UCL with a thinner thickness of shell compared to only an active layer, which is favorable for FRET applications, especially for PDT.

To acquire a highly efficient UCL for UCNPs, the arrangement of Nd^{3+} as sensitizers was also optimized. The maximal intensity was reached at a concentration of ~20% Nd^{3+} (Fig. 2e and f). The UCL intensity declined at higher concentrations of Nd^{3+}, which may be ascribed to the more seriously cross-relaxation occurring among Nd^{3+} ions. Moreover, a higher concentration of Nd^{3+} ions also resulted in more serious quenching effects to Ho^{3+} (Fig. S7†), which limits the doped concentration of Nd^{3+} ions.

Until now, we have reported a highly efficient core–shell–shell structure for UCL with an excitation of 808 nm, but the FRET efficiency should also be considered when UCNPs are used for FRET-based biological applications, such as PDT. For PDT, the yield of $^1O_2$ generation is determined by two factors: the excitation intensity on organic photosensitizers and the FRET efficiency from UCNPs to organic photosensitizers. However, the shell thickness has two opposing effects on the above two factors. A thicker shell facilitates UCL, resulting in a more effective excitation of the photosensitizer, *e.g.* Rose Bengal (RB). On the other hand, it reduces the FRET efficiency due to the increase in the transfer distance between the luminescent Ho^{3+} ions in the core and RB. Therefore, a trade-off between the two conflicting requirements has to be reached for the optimal generation of $^1O_2$. For this reason, we synthesized different samples with various active-shell thicknesses to determine an optimum thickness. All the samples had the same ion concentration, *i.e.* 8 mol% Yb^{3+} and 1 mol% Ho^{3+} in the core and 20 mol% Nd^{3+} in the active layer. Samples A, B, C and D had nearly the same size core and the same inert layer thickness, but different thicknesses of the active layer: A (0.4 nm active layer, Fig. S8†), B (1 nm active layer, Fig. S9†), C (2.5 nm active layer, Fig. S10†), and D (4.2 nm active layer, Fig. S11†). The UCL increased in intensity with the increase in the active layer thickness due to more light being harvested by more Nd^{3+} ions (Fig. S12†).

To acquire a high FRET efficiency, the UCNPs need be covalently coupled with organic photosensitizers, *e.g.* RB. Similar to our previous report,[23] we functionalized the nanoparticles and the process is shown in Fig. 1d. We firstly transferred the

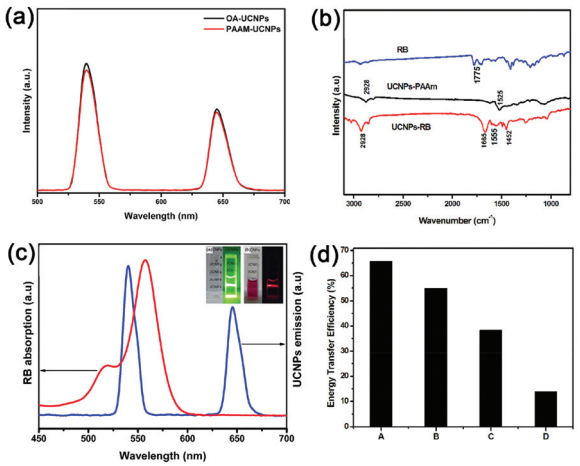

Fig. 3 (a) Upconversion spectra of the UCNPs before and after phase transfer. (b) Infrared absorption spectra of free RB, PAAm–UCNPs and RB–UCNPs. (c) Spectral overlap between the emission spectrum of the donor (UCNPs) (blue line) and the absorption spectrum of the acceptor (RB) (red line). (d) Energy transfer efficiency of the four UCNPs–RB samples A–D (A = 0.4 nm, B = 1.5 nm, C = 2.6 nm and D = 4.2 nm active layer thicknesses).

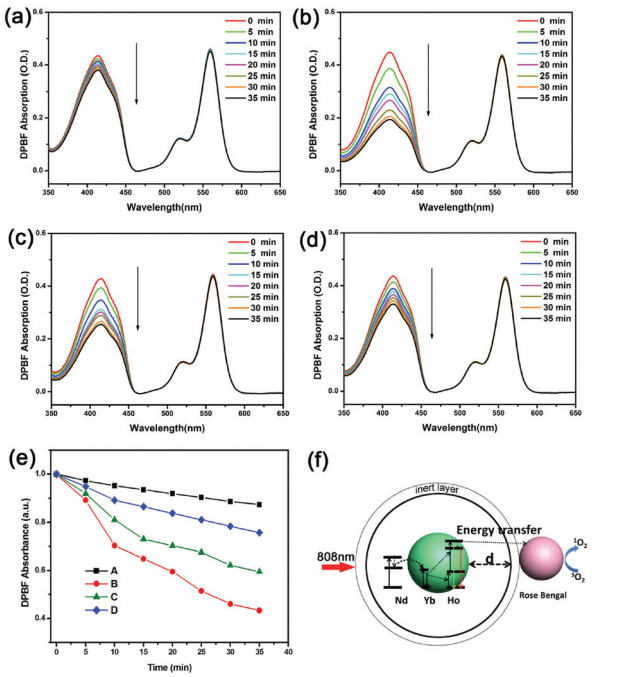

Fig. 4 Absorption spectra measured every 5 minutes of DPBF (10 μL, 8 mM) incubated with $NaYF_4$:Yb/Ho(8/1%)@$NaYF_4$:Nd (20%)@$NaYF_4$ with different $NaYF_4$:Nd(20%) active-shell thicknesses under irradiation at 808 nm: (a) sample A (0.4 nm); (b) sample B (1.6 nm); (c) sample C (2.5 nm); (d) sample D (4.2 nm). (e) Absorbance at 410 nm of DPBF in ethanol solutions of A–D as a function of irradiation time. (f) Illustrated diagram showing the different $NaYF_4$:Nd(20%) active-layer thicknesses of the nanoparticles for the production of $^1O_2$.

UCNPs to an aqueous solution without any significant change in the UCL (Fig. 3a). Afterwards, the water soluble amine-functionalized UCNPs were covalently linked with RB through a traditional 1-ethyl-3-(3-dimethylaminopropyl) carbodiimide hydrochloride (EDC) coupling reaction (ESI, Experimental section†). The formed amide bonds were confirmed by infrared absorption spectra (Fig. 3b). The C═O at 1775 cm^{-1} confirmed the stretching vibration mode of the carboxyl group in RB (Fig. 3b, top). After PAAm phase transfer, there was a peak at 1525 cm^{-1}, which is attributed to N–H stretching vibration modes (Fig. 3b, middle). Finally, after conjugating with RB, the peak at 1525 cm^{-1} disappeared and two new peaks around 1665 cm^{-1} and 1452 cm^{-1} appeared, which suggested C═O bending vibration and C–N stretching vibration modes. The peak at 1555 cm^{-1} is ascribed to the N–H bending vibration mode (Fig. 3b, bottom). All the absorptions at 2928 cm^{-1} indicate oleic acid C–H stretching vibration modes. After covalently coupling with RB, the green emission of the UCNPs quenched significantly (Fig. 3c, top right corner). This indicates the presence of FRET from the UCNPs to RB, which is due to the spectral overlap of RB and UCNPs (Fig. 3c). The FRET efficiency can be measured experimentally and is commonly defined as:[27] $E = (I_0 - I_1)/I_0$, where I_0 and I_1 are the green emission intensities of the UCNPs before and after covalently linking with RB, respectively. The FRET efficiency gradually decreased from sample A (65.7%) to D (13.8%) with increasing active layer thickness owing to the longer distance between the UCNPs and RB molecules as we anticipated (Fig. 3d and S13†).

The results above certainly demonstrate that the active shell has two opposing effects on the UCL and FRET efficiency, and therefore an optimum thickness exists to produce the highest yield of $^1O_2$. Fig. 4f show a schematic design for different thicknesses of $NaYF_4$:Nd(20%) active-shell covalently bound to Rose Bengal for production of $^1O_2$. The optimum thickness of the active layer was determined through the generation of $^1O_2$ from the UCNPs–RB conjugation with 808 nm irradiation. We used the traditional chemical probe of 1,3-diphenylisobenzofuran (DPBF)[25] to identify the generation of $^1O_2$. The decrease in absorption (~417 nm) of DPBF is proportional to the production of $^1O_2$. Fig. 4a–d show the absorption spectra measured every 5 minutes for four UCNPs–RB samples (2 mg mL^{-1}) incubated with DPBF (10 μL, 8 mM) under irradiation at 808 nm. Absorption decreases at 417 nm were observed for all the samples, showing increases in the presence of $^1O_2$. Sample B with a shell thickness of 1.5 nm was the best for $^1O_2$ production, followed by C, D and then A (Fig. 4e). Although sample B showed neither the strongest upconversion emission nor the highest energy transfer efficiency, the largest production of $^1O_2$ was by sample B, which properly balanced the UCL intensity and the FRET efficiency.

Before applying these UCNPs to biological applications, the heating effect should be evaluated with the 808 nm laser to find the safe power density for biological applications. For UCNPs-based PDT, the biggest problem is that the excitation light of 980 nm is at the rising edge of the absorption of tissue (although much lower than visible light) and can be strongly absorbed by water (Fig. 5a). The laser induced heating effect

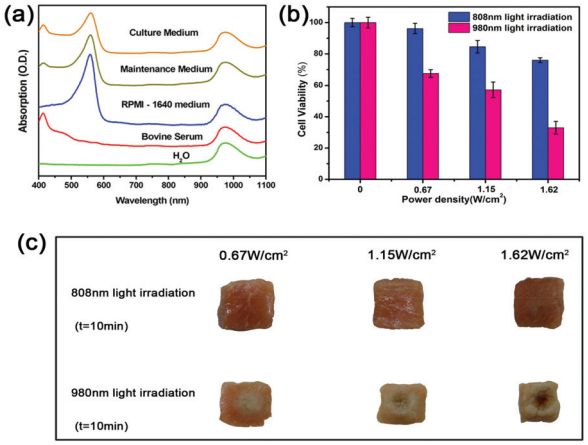

Fig. 5 (a) Absorption spectra of water, bovine serum, RPMI-1640 medium cell culture, maintenance medium (1% bovine serum and 99% RPMI-1640), and cell culture medium (2% bovine serum and 98% RPMI-1640). (b) Heating effects of 808 nm and 980 nm lasers evaluated by the viability of HeLa cancer cells. (c) Morphology changes in pork tissue after continuous irradiation by an 808 nm laser and a 980 nm laser for 10 minutes at the same power density.

was evaluated using the viability of HeLa cells irradiated at different power densities. The cell viability was measured by thiazolyl blue tetrazolium bromide (MTT) (Fig. 5b).[28] After irradiating for 10 minutes using an 808 nm laser, the cell survival rate was 68.54% at 1.62 W cm^{-2} and 95.17% at 0.67 W cm^{-2}. Hence the appropriate power density of irradiation with an 808 nm laser is about 0.67 W cm^{-2}. In contrast, the cell survival rate was only 51% at 1.62 W cm^{-2} and 65.48% at 0.67 W cm^{-2} after irradiating for 10 minutes using a 980 nm laser, indicating the much lower overheating effect for cells irradiated with an 808 nm laser. This low overheating effect from 808 nm irradiation was further confirmed by the morphology changes in pork tissue after irradiating for 10 minutes (Fig. 5c).

The red emission of the UCNPs at 650 nm could be exploited for bioimaging purposes, to fulfil photodynamic diagnosis and PDT simultaneously. The nuclei of HeLa cells and human alveolar adenocarcinoma (A549) cells stained with 4,6-diamidino-2-phenylindole (DAPI) showed a blue color (Fig. 6, left). The red emission resulted from the UCNPs–RB upon excitation with 808 nm light. Fig. 6 (top row) shows the bright red emission around the nuclei region, indicating the UCNPs–RB/FA had entered into the HeLa cells. For comparison, a control group, which was HeLa cells saturated with UCNPs–RB without linking FA, did not show a bright UCL (Fig. 6, middle). The A549 cells, which are poor in expressing the folate receptor, were incubated with the same concentration of drugs (UCNPs–RB/FA), and showed nearly no red fluorescence (Fig. 6, bottom). More importantly, benefiting from the deep penetration depth of red light emission, UCNPs–RB/FA have the potential for use in image-guided PDT applications.

The *in vitro* PDT effect of the UCNPs was assessed by cell viability. From the absorption spectrum, it was observed that the maximum amount of RB per nanoparticle was about 94

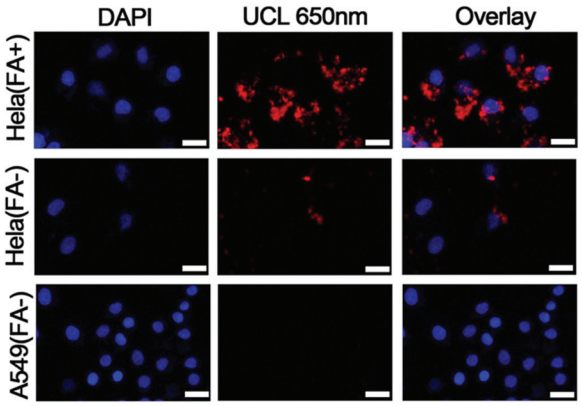

Fig. 6 UCL 650 nm images and specificity of UCNPs–RB/FA nanoconstructs under excitation with an 808 nm laser. HeLa cells cultured in folate-free medium (positive, top) and in folate-supplemented medium (negative, middle). A negative control was also performed with A549 cells (negative, bottom). From left to right, DAPI-stained cell nuclei, UCL 650 nm and overlay images. All scale bars are 20 μm.

(Fig. S14†). After incubation with different concentrations of UCNPs–RB/FA for 24 h, the HeLa cells were irradiated for 10 minutes using an 808 nm laser. The cell viability dramatically decreased, while the cells that were not irradiated did not show any significant change (Fig. 7). This indicates that cell death was dominated by the PDT effect of RB activated by the UCNPs. When the concentration of Nd^{3+}–UCNPs–RB was 200 μg mL^{-1} (cell viability was ~85% without irradiation), nearly 44.5% of the HeLa cells were killed by PDT. The therapeutic effects nearly reached the level of our previous report,[15] which performed UCNPs-based PDT with the same photosensitizer (Rose Bengal) under 980 nm irradiation. In contrast, during the PDT process with 808 nm irradiation, we can irradiate cells or tissue without any interval to avoid the overheating effects. Thus, the Nd^{3+}–UCNPs with the optimum shell thickness have great potential in bioimaging-guided PDT with

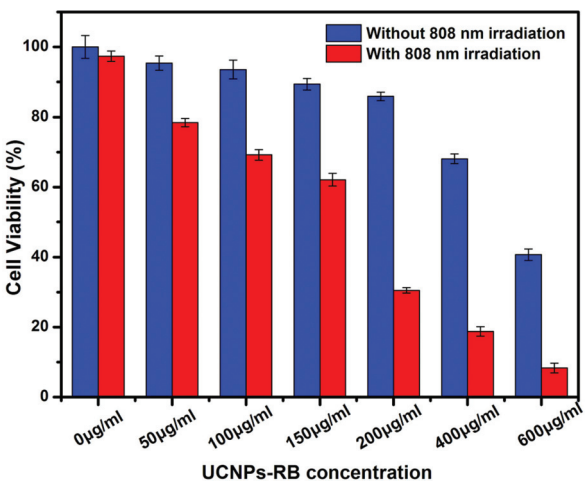

Fig. 7 Viability of HeLa cancer cells incubated with different concentrations of UCNPs–RB with (0.67 W cm^{-2}) (red histogram) and without (blue histogram) 808 nm laser irradiation.

808 nm laser irradiation, and may make PDT a more practical method for tumor therapy.

4. Conclusions

In summary, $NaYF_4$:Yb/Ho@$NaYF_4$:Nd@$NaYF_4$ core–shell–shell nanoparticles have been constructed and optimized, with the aim of developing luminescence upconversion nanostructures that can be activated with 808 nm light for FRET-based applications, especially PDT. A trade-off between the robust upconversion emission and the efficient transfer of excitation energy from the nanoparticles to the photosensitizers was reached. An inert layer was particularly effective to offset the loss due to the shortening of the active layer. A proof of concept test was performed for cell imaging and PDT simultaneously with HeLa cells under excitation at 808 nm, where minimization of the overheating effect was confirmed from a comparison with the popular excitation wavelength of 980 nm.

Acknowledgements

This work was financially supported by NSF of China (11174277, 11374297, 61275202, 21304084, 11474278 and 51372096), a joint research program between CAS of China and KNAW of the Netherlands, the IOP program of the Netherlands, and the John van Geuns foundation.

Notes and references

1 J. Wang, R. Deng, M. A. MacDonald, B. Chen, J. Yuan, F. Wang, D. Chi, T. S. A. Hor, P. Zhang and G. Liu, *Nat. Mater.*, 2014, **13**, 157–162.
2 D. J. Gargas, E. M. Chan, A. D. Ostrowski, S. Aloni, M. V. P. Altoe, E. S. Barnard, B. Sanii, J. J. Urban, D. J. Milliron and B. E. Cohen, *Nat. Nanotechnol.*, 2014, **9**, 300–305.
3 F. Wang and X. Liu, *Acc. Chem. Res.*, 2014, **47**, 1378–1385.
4 W.-P. Qin, Z.-Y. Liu, C.-N. Sin, C.-F. Wu, G.-S. Qin, Z. Chen and K.-Z. Zheng, *Light: Sci. Appl.*, 2014, **3**, e193.
5 W. Zou, C. Visser, J. A. Maduro, M. S. Pshenichnikov and J. C. Hummelen, *Nat. Photonics*, 2012, **6**, 560–564.
6 X. Xie and X. Liu, *Nat. Mater.*, 2012, **11**, 842–843.
7 G. Chen, J. Shen, T. Y. Ohulchanskyy, N. J. Patel, A. Kutikov, Z. Li, J. Song, R. K. Pandey, H. Ågren and P. N. Prasad, *ACS Nano*, 2012, **6**, 8280–8287.
8 L. Zhou, Z. Li, Z. Liu, M. Yin, J. Ren and X. Qu, *Nanoscale*, 2014, **6**, 1445–1452.
9 Y. Liu, D. Tu, H. Zhu, E. Ma and X. Chen, *Nanoscale*, 2013, **5**, 1369–1384.
10 Y. Zhou, S.-T. Han, X. Chen, F. Wang, Y.-B. Tang and V. Roy, *Nat. Commun.*, 2014, 5, DOI: 10.1038/ncomms5720.
11 T. Wu, M. Barker, K. M. Arafeh, J.-C. Boyer, C.-J. Carling and N. R. Branda, *Angew. Chem., Int. Ed.*, 2013, **52**, 11106–11109.
12 D. Tu, L. Liu, Q. Ju, Y. Liu, H. Zhu, R. Li and X. Chen, *Angew. Chem., Int. Ed.*, 2011, **50**, 6306–6310.
13 N. M. Idris, M. K. Gnanasammandhan, J. Zhang, P. C. Ho, R. Mahendran and Y. Zhang, *Nat. Med.*, 2012, **18**, 1580–1585.
14 Q. Zhan, J. Qian, H. Liang, G. Somesfalean, D. Wang, S. He, Z. Zhang and S. Andersson-Engels, *ACS Nano*, 2011, **5**, 3744–3757.
15 J. Shen, G. Chen, A. M. Vu, W. Fan, O. S. Bilsel, C. C. Chang and G. Han, *Adv. Opt. Mater.*, 2013, **1**, 644–650.
16 Y.-F. Wang, G.-Y. Liu, L.-D. Sun, J.-W. Xiao, J.-C. Zhou and C.-H. Yan, *ACS Nano*, 2013, **7**, 7200–7206.
17 X. Xie, N. Gao, R. Deng, Q. Sun, Q. Xu and X. Liu, *J. Am. Chem. Soc.*, 2013, **135**, 12608–12611.
18 H. Wen, H. Zhu, X. Chen, T. F. Hung, B. Wang, G. Zhu, S. F. Yu and F. Wang, *Angew. Chem., Int. Ed.*, 2013, **52**, 13419–13423.
19 Y. Zhong, G. Tian, Z. Gu, Y. Yang, L. Gu, Y. Zhao, Y. Ma and J. Yao, *Adv. Mater.*, 2014, **26**, 2831–2837.
20 Y. Wang, K. Liu, X. Liu, K. Dohnalová, T. Gregorkiewicz, X. Kong, M. C. Aalders, W. J. Buma and H. Zhang, *J. Phys. Chem. Lett.*, 2011, **2**, 2083–2088.
21 N. J. Johnson, A. Korinek, C. Dong and F. C. van Veggel, *J. Am. Chem. Soc.*, 2012, **134**, 11068–11071.
22 G. H. Dieke and B. Pandey, *J. Chem. Phys.*, 1964, **41**, 1952–1969.
23 K. Liu, X. Liu, Q. Zeng, Y. Zhang, L. Tu, T. Liu, X. Kong, Y. Wang, F. Cao and S. A. Lambrechts, *ACS Nano*, 2012, **6**, 4054–4062.
24 J. J. Lamberts, D. R. Schumacher and D. Neckers, *J. Am. Chem. Soc.*, 1984, **106**, 5879–5883.
25 P. B. Merkel and D. R. Kearns, *J. Am. Chem. Soc.*, 1975, **97**, 462–463.
26 F. Wang, J. Wang and X. Liu, *Angew. Chem., Int. Ed.*, 2010, **49**, 7456–7460.
27 J. R. Lakowicz, *Principles of fluorescence spectroscopy*, Springer, 2007.
28 D. Gerlier and N. Thomasset, *J. Immunol. Methods*, 1986, **94**, 57–63.